Contents lists available at ScienceDirect

Surface & Coatings Technology

journal homepage: www.elsevier.com/locate/surfcoat

CrossMark

Growth and characterization of chromium carbide films deposited by high rate reactive magnetron sputtering for electrical contact applications

Kristian Nygren [a,b,*], Mattias Samuelsson [b], Axel Flink [b], Henrik Ljungcrantz [b], Åsa Kassman Rudolphi [c], Ulf Jansson [a]

[a] *Uppsala University, Department of Chemistry - Ångström Laboratory, Box 538, SE-751 21 Uppsala, Sweden*
[b] *Impact Coatings AB, Westmansgatan 29, SE-582 16 Linköping, Sweden*
[c] *Uppsala University, Department of Engineering Sciences, Box 534, SE-751 21 Uppsala, Sweden*

ARTICLE INFO

ABSTRACT

Chromium carbide films with different phase contents were deposited at 126 ± 26 °C by industrial high rate reactive magnetron sputtering, using both direct current magnetron sputtering (DCMS) and high power impulse magnetron sputtering (HiPIMS). Film structure and properties were studied by SEM, XRD, TEM, XPS, NRA, Raman spectroscopy, nanoindentation, unlubricated reciprocating sliding experiments, and a laboratory setup to measure electrical contact resistance. The films consisted of amorphous a-CrC_y, a nanocrystalline minority phase of metastable cubic nc-CrC_x, and a hydrogenated graphite-like amorphous carbon matrix (a-C:H). The DCMS and HiPIMS processes yielded films with similar phase contents and microstructures, as well as similar functional properties. Low elastic modulus, down to 66 GPa, indicated good wear properties via a hardness/elastic modulus (H/E) ratio of 0.087. Unlubricated steady-state friction coefficients down to 0.13 were obtained for films with 69 at.% carbon, while the electrical contact resistance could be reduced by two orders of magnitude by addition of a-C:H phase to purely carbidic films. The present films are promising candidates for sliding electrical contact applications.

© 2014 The Authors. Published by Elsevier B.V. This is an open access article under the CC BY license (http://creativecommons.org/licenses/by/3.0/).

1. Introduction

Sliding electrical contacts play an important part in everyday life. Most materials used today are expensive noble metals or alloys, like Au, Pd, and Au–Co, which are applied as thin films on a conductive substrate. More cost-effective alternatives are base metals and alloys, such as Ti and stainless steel, but they more easily form high resistance surface oxides [1], requiring high contact forces to break through. Such forces cause severe wear and are unsuitable in e.g. consumer electronics. This can be improved by using soft metals, such as Ag, but they will exhibit severe wear even at low contact force [2], leading to reduced reliability and shortened product life. A thicker film, adding to the product cost, is then required to compensate for the loss of metal. Thus, there is a driving force to design new films with lower cost and improved material properties.

Replacing noble metals with nanocomposite transition metal carbide/amorphous carbon (Me–C/a-C) films, with nanocrystalline carbide grains embedded in an amorphous carbon matrix, is a proposed alternative [3]. The carbon matrix adds a polymeric-like character with high hardness/elastic modulus ratio and low surface energy [4], providing reduced friction and improved wear properties by the formation of graphite-like tribofilms. Meanwhile, the carbide phase retains its high hardness, low resistivity, and high corrosion resistance.

Several studies on various carbide-based nanocomposites, e.g. Ti–C [5], Ti–Ni–C [6], Ti–Si–C [7], Ti–(Si, Ge, Sn)–C–Ag [8,9], Ti–Si–C–Ag–Pd [10], and Nb–C [11], have demonstrated promising properties and potential use in electrical contact applications. However, the Cr–C system has some unique properties which are interesting for a new contact material. Perhaps the most striking property is that Cr–C has a high glass forming ability and a wide glass forming range compared to other Me–C systems [12], meaning that an amorphous structure can be obtained over a wide range of experimental conditions and film compositions. This behavior makes it possible to co-sputter nanocomposite a-CrC_y/a-C films with separate phases of amorphous carbide and amorphous carbon, making the films soft yet reasonably conductive [13,14]. It is also possible to sputter nanocrystalline nanocomposites [15–17], and this microstructural window offers great potential to tailor the functional film properties. Some studies have reported high hardness and very low electrical resistivity for Cr-rich Cr–C films [15,18,19],

* Corresponding author at: Uppsala University, Department of Chemistry - Ångström Laboratory, Box 538, SE-751 21 Uppsala, Sweden. Tel.: +46 13 359520; fax: +46 18 513548.
E-mail address: kristian.nygren@kemi.uu.se (K. Nygren).

although in a sliding contact application such films are unlikely to perform well due to high coefficients of friction [20]. A nanocomposite structure, on the other hand, notably reduces friction and improves wear properties [16,20–22]. Moreover, Cr–C/a-C films were recently shown to be protected from deep oxidation by an extremely thin Cr oxide film, where the a-C phase reduced surface concentrations of oxidized Cr by nearly 50% [17]. However, no one has studied Cr–C/a-C films for the purpose of electrical contact applications.

The aim of this study is to investigate the structural, mechanical, tribological, and electrical contact properties of Cr–C films deposited by high rate reactive magnetron sputtering at low substrate temperature. Although direct current magnetron sputtering (DCMS) offers high deposition rates, the method can lead to low-density films with hampered functional properties. Therefore, films grown by high power impulse magnetron sputtering (HiPIMS) were also studied. HiPIMS provides a higher degree of ions in the deposition flux, which can lead to denser films with smoother surface and better functional properties, however at the cost of reduced deposition rate [23]. In this study, the two sputtering methods, different reactive gas flows, and two substrate bias potentials were used to deposit Cr–C films with different compositions. Relationships between deposition conditions, composition, structure, chemical bonding, and functional properties are established.

2. Experimental details

Cr–C films were deposited using an InlineCoater™ 500 (Impact Coatings AB, Sweden), which is an industrial short-cycle high vacuum physical vapor deposition system (details are given elsewhere [24]). The base pressure was 1.3×10^{-4} Pa. One unbalanced magnetron was mounted on the second process chamber for single-sided top-down deposition geometry with a perpendicular target-to-substrate distance of 15 cm. The sputtering target consisted of industrial grade Cr (rectangular 898 cm^2, purity at least 99.7 at.% Cr). All depositions were made by DCMS or HiPIMS. In the case of DCMS, the electric current density was 0.022 A cm^{-2} and the target potential was 450–550 V. In the case of HiPIMS, the peak electric current density was 0.40–0.50 A cm^{-2}, the target potential was adjusted to yield an average power of 5 kW, the pulse frequency was 500 Hz, and the pulse width was 100 μs. The target was pre-sputtered for 3 min prior to each experiment. Metallic operation was confirmed by stable plasma emission intensity from a Cr line and by stable electrical potential (500 V) of the magnetron in constant current mode (20 A). Substrates of Si and SS316L polished to a mirror-like surface finish were placed flat down on a Cr-coated stainless steel fixture with a mass of 10 kg. The starting temperature of the fixture was 126 ± 26 °C for each batch, and process-induced heat increased the temperature during deposition to 148 ± 18 °C. Film deposition was preceded by Ar plasma etching for 2 min at 1.9 Pa by applying unipolar potential pulses with an amplitude of −700 V, a frequency of 250 kHz, and a pulse width of 1.6 μs. A thin Cr layer (80–100 nm) was deposited at 1.1 Pa to improve adhesion and to deposit the carbide films on chemically similar surfaces. Different C$_2$H$_2$ gas flow rates (0–78 sccm) were used to control film composition. Typical reactive process pressure was 1.1–1.5 Pa. Process time was adjusted to obtain a similar film thickness (1.29 ± 0.18 μm). A constant substrate bias potential (U_b) of −50 V was normally applied. Some films were deposited at $U_b = −150$ V in order to more strongly differentiate the DCMS and HiPIMS processes.

Film microstructure was studied by grazing incidence X-ray diffraction (GIXRD), using a diffractometer equipped with a Cu $K\alpha$ radiation source and parallel beam geometry, and transmission electron microscopy (TEM), using a FEI Tecnai G^2 TF 20 UT microscope operated at 200 kV. Cross-sectional TEM samples were prepared using a Zeiss ES-1540 Crossbeam FIB using Ga-ions with the so-called lift-out technique [25]. Film cross-sections and surfaces were studied using a Leo 1550 field emission scanning electron microscope (SEM) with an electron gun potential of 10 kV. Film composition and chemical binding energies

were determined by X-ray photoelectron spectroscopy (XPS), using a PHI Quantum 2000 spectrometer with monochromatic Al $K\alpha$ radiation. XPS sensitivity factors were calibrated by elastic recoil detection analysis of reference samples and the measurement accuracy for this method is typically a few atomic percent. High resolution C1s, Cr2p and O1s spectra with a step size of 0.05 eV were obtained using a pass energy of 11.75 eV. Pre-sputtering was performed to depths of both ~8 and ~15 nm at different film spots, using 0.2 keV Ar$^+$ for 75 min and 0.5 keV Ar$^+$ for 20 min, respectively, to remove surface contamination. The Ar$^+$ ion incidence angle was 45°. There was no significant difference in composition between the two measurements. The average composition of each film is reported with a precision of ±2 at.%. Depth profiles obtained using 4 keV Ar$^+$ resulted in lower carbon contents (4–12 at.%, 95% CI), similar to previous results [17], and were only used to confirm that there was no major deviation in bulk composition. Chemical bonding is reported based on pre-sputtering using 0.2 keV Ar$^+$ to minimize sputter damages [26]. Hydrogen content was analyzed by nuclear reaction analysis (NRA) using a beam energy of 6.8 MeV to obtain bulk information. Film composition will generally be discussed without the relative contribution of hydrogen. The structure of the carbon phase was studied by Raman spectroscopy, using a Renishaw Micro Raman 2000 spectrometer with a 514.5 nm Ar laser operated at 25 mW.

Friction properties were studied by unlubricated reciprocating experiments in a standard indoor environment (22 °C, RH = 42%) using ball bearing 100Cr6 steel balls with a diameter of 10 mm. The normal load was 5.0 N, the stroke amplitude was 10 mm, and the frequency was 2.0 Hz. Mechanical film properties were studied by nanoindentation, using a CSM Instruments Ultra Nano Indenter XP. The indenting part was a diamond Berkovich tip exerting a maximum load of 1200 μN, which resulted in penetration depths of 60–100 nm. Electrical contact resistance was basically measured in a four-wire setup, using an Au/Ni probe (∅ = 1.2 mm), further described elsewhere [9]. The software was improved to acquire average contact resistance in a steady state, defined as a relative difference in resistance smaller than 3% for a minimum of three consecutive measurements. Contact force was 1.00 ± 0.01 N. At least 3 measurements, in different spots, were made for each film.

3. Results

3.1. Film composition and deposition rates

A series of chromium carbide films with total carbon content ranging from 19 to 69 at.% were deposited. Oxygen content was determined to be 3 at.%, which is an acceptable level for a high vacuum chamber. NRA was only performed for one DCMS and one HiPIMS sample, both with a C/Cr ratio of about 1.3. The hydrogen content in both films was determined to be 1.3 wt.% H, corresponding to an atomic H/C ratio = $0.68 \approx 2/3$. It is likely, however, that the hydrogen content should vary with carbon content in the film and further studies are required to establish the variation in H/C ratio at different compositions.

The deposition rates for pure Cr (no added C$_2$H$_2$ gas) were 480 nm·min^{-1} and 125 nm·min^{-1} for the DCMS and HiPIMS processes, respectively. The addition of C$_2$H$_2$ gas reduced deposition rates significantly. Typically, deposition rates for films with a carbon content of 20–40 at.% C, or more, were 60% lower than those for pure Cr films. The reduction in deposition rate with addition of C$_2$H$_2$ gas to the discharge can be explained by the formation of carbon-containing compounds on the target surface, and these compounds will sputter at a lower rate compared to Cr [27].

The DCMS and HiPIMS processes were carried out at different current densities and in the case of HiPIMS with a pulsing frequency. It is therefore difficult to directly compare the two processes with respect to their conversion efficiency of the C$_2$H$_2$ gas. From the gas flow rates and target currents, it is possible to calculate the number of C$_2$H$_2$ gas molecules per electric charge which was required to give a certain film composition. The gas flow rate can be expressed as the number of gas molecules per second $\dot{n}$ (s^{-1}) according to Eq. (1), where $\dot{V}$ is the

gas flow rate ($cm^3 min^{-1}$), N_A is the Avogadro constant (mol^{-1}), and V_m is the molar volume ($L mol^{-1}$) of an ideal gas at 1 atm of pressure and 273.15 K.

$$\dot{n} = \dot{V} \times \frac{N_A}{V_m \times 10^3 \left[\frac{cm^3}{L}\right] \times 60\left[\frac{s}{min}\right]} \quad (1)$$

The magnetron current I (in A) can be expressed as elementary charges per second following that $1\ C\ s^{-1} \approx 6.242 \times 10^{18}\ e\ s^{-1}$. The number of C_2H_2 gas molecules per electric charge is then obtained from Eq. (2).

$$\frac{number\ of\ C_2H_2\ gas\ molecules}{electric\ charge} = \frac{\dot{n}}{I \times 6.242 \times 10^{18}} \left[e^{-1}\right] \quad (2)$$

As can be seen in Fig. 1, the HiPIMS process is more efficiently using the feed gas to give films with specific carbon content. This can be explained by the formation of more carbon radicals [28], which can be deposited directly from the plasma onto the growing film without ever forming a compound on the sputter target. Gas disassociation, and therefore formation of carbon radicals, is fostered by the higher plasma density for HiPIMS [29].

3.2. Film microstructure and chemical bonding

3.2.1. Scanning electron microscopy

Fig. 2 illustrates surface morphologies for Cr–C films with different total carbon contents deposited on SS316L. Panels a and b in Fig. 2 show a nodular surface morphology for films with carbon contents of 26 and 19 at.% C, respectively. Nodules were smaller for the HiPIMS film (Fig. 2b), about 15 nm, compared to a typical nodule size of about 30 nm in the DCMS film (Fig. 2a). These results were obtained from digitally edge-enhanced images, shown as insets in Fig. 2, and similar results were obtained for un-altered images. At higher carbon contents (56 at.%), the surface morphology was more disordered (Fig. 2c). No clear difference in surface morphology between the DCMS and HiPIMS films was observed. An increase in U_b to -150 V leads to a more refined surface morphology (Fig. 2d), which can be explained by the higher ion bombardment energies [30]. Fig. 3 shows cross-section morphologies for fractured Cr–C films with 56 at.% C deposited on Si with a Cr adhesion layer. The DCMS film deposited at $U_b = -50$ V exhibited a typical columnar microstructure, frequently observed in magnetron sputtered Me–C films (Fig. 3a). The columnar structure decreases with an increase
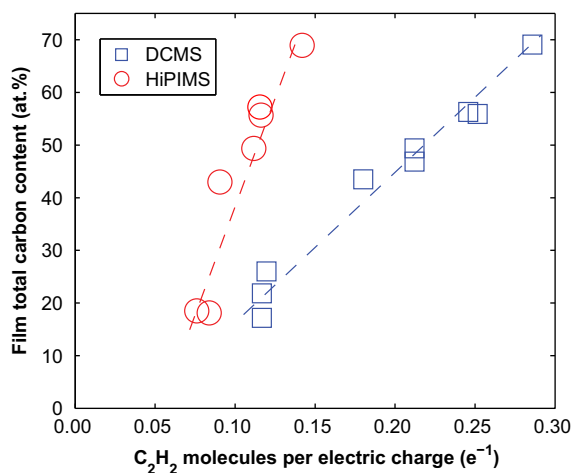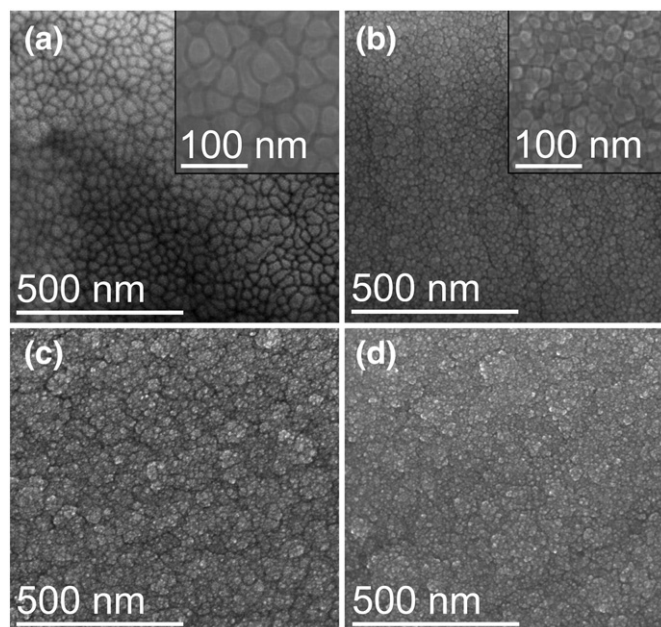

Fig. 2. SEM images of Cr–C films deposited on SS316L. Letters correspond to films deposited by (a) DCMS with 26 at.% C at a substrate bias potential (U_b) of -50 V, (b) HiPIMS with 19 at.% C at $U_b = -50$ V, (c) DCMS with 56 at.% C at $U_b = -50$ V, and (d) DCMS with 56 at.% C at $U_b = -150$ V. The insets in (a) and (b) have been digitally enhanced to emphasize the edges.

in U_b to -150 V (Fig. 3c). The HiPIMS film deposited at $U_b = -50$ V exhibits a clearly less columnar structure than the corresponding DCMS film (Fig. 3b), and an increase in U_b to -150 V promoted an even denser structure (Fig. 3d). The differences in morphology are likely related to a denser microstructure, owing to higher average ion energy for HiPIMS [31]. Similar differences in columnar growth between DCMS and HiPIMS have been reported by Greczynski et al. [32] for reactively sputtered Cr–N films.

3.2.2. X-ray diffraction

GIXRD diffractograms for Cr–C films with different carbon contents are shown in Fig. 4. As can be seen, all diffractograms show a broad feature at $2\theta \sim 40$–$45°$. This suggests that the films mainly are amorphous in agreement with many earlier studies [13,14,17,33]. For the DCMS film with 26 at.% C, this feature forms a sharper, more intense peak at $2\theta \sim 44°$. In addition, this film shows a broad, less intense feature at $2\theta \sim 56°$. The two peaks can be attributed to a cubic CrC_x phase with NaCl structure. This phase is not thermodynamically stable, but has been observed in some earlier studies on sputtered Cr–C films [21,34]. The most carbon-rich films with 69 at.% C have very low intensities of these peaks, which correspond to the typical reduction in grain size when increasing the carbon content [35]. With an increase in U_b to -150 V, the DCMS film with 56 at.% C shows four weak features at 38°, 44°, and 65°, as well as one at 56°. All of them can be attributed to the (111), (200), (220), and (211) peaks from cubic (NaCl) CrC_x, respectively [36]. Additionally there is a very weak feature at about 80° which stems from the cubic (222) and (311) reflections. The lattice parameter was determined to be 4.08 Å, which is in good agreement with the value of 4.13 Å reported by Dai et al. [37] for cubic CrC_x films deposited by reactive DCMS. In conclusion, the XRD results show that the films are mainly amorphous, although they also contain some metastable cubic CrC_x.

3.2.3. Transmission electron microscopy

Films with 56 at.% carbon were analyzed by TEM. Fig. 5 shows the TEM images and inset SAED patterns for one DCMS film and one HiPIMS film. The low magnification images (Fig. 5a and b) reveal a
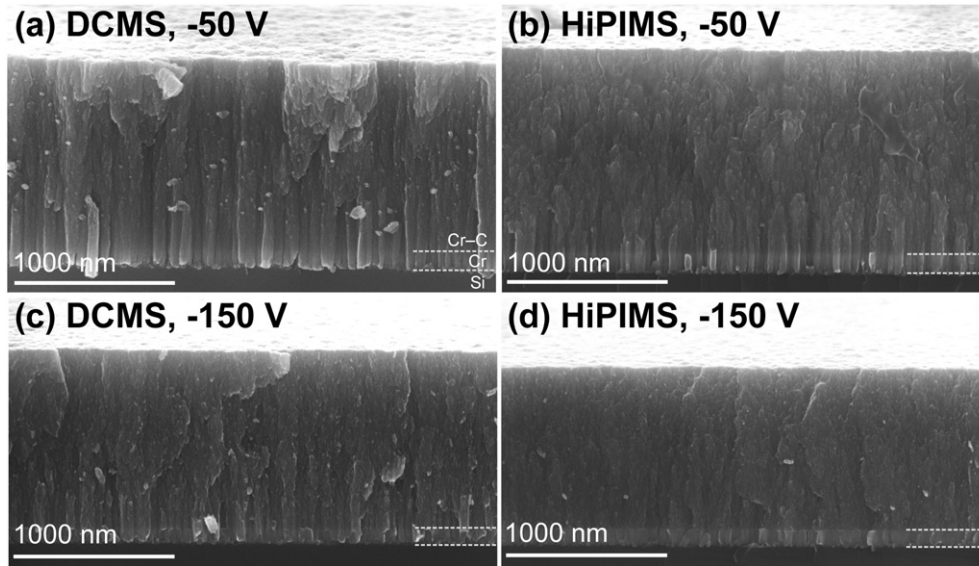

Fig. 1. Total carbon content in Cr–C films vs. the number of C_2H_2 gas molecules per electric charge unit (corresponding to sccm/A) for DCMS and HiPIMS. Film composition was determined by XPS. The dashed lines are guides for the eye.

Fig. 3. SEM cross-sections of fractured Cr–C films with 56 at.% C deposited on Si substrates with Cr adhesion layers. Letters correspond to films deposited by (a) DCMS at a substrate bias potential (U_b) of -50 V, (b) HiPIMS at $U_b = -50$ V, (c) DCMS at $U_b = -150$ V, and (d) HiPIMS at $U_b = -150$ V.

microstructure with elongated features parallel to the substrate normal, clearly illustrating the growth direction. Both bright and dark areas are seen, suggesting regions rich in carbon and chromium, respectively, based on elemental contrast. In Fig. 5c and d, images with higher magnification show that these regions are about 5 nm in size. No differences between the two DCMS and HiPIMS films were found, and this was concluded after numerical evaluations of relative intensities in high magnification TEM images corresponding to an area of 7100 nm^2 for each film.
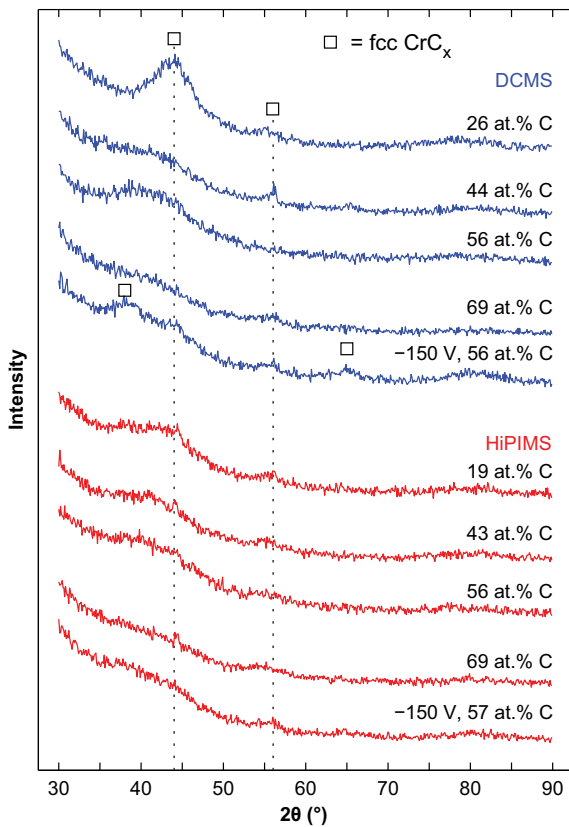

Fig. 4. GIXRD diffractograms obtained at 1° incidence angle for Cr–C films with different total carbon contents deposited by DCMS (top five) and HiPIMS (bottom five). Films were deposited at a substrate bias potential (U_b) of -50 V unless marked differently.

Most areas revealed no apparent crystalline order, corresponding to an amorphous structure. Nonetheless, some aligned lattice planes were found and in particular in one area for the HiPIMS film. This specific area is illustrated in Fig. 5d, where one unusually large cubic CrC_x grain, 3 nm in size, has been marked by white circle. The nanocrystalline phase content is roughly estimated to be less than 10% by area quantification of amorphous and nanocrystalline regions in the TEM images.

The SAED pattern (inset in Fig. 5c) for the DCMS film is typical of amorphous Cr–C films [13,14,38], showing diffuse rings with radii corresponding to the average distance between neighboring atoms rather than the conventional d-spacing between ordered lattice planes [34]. Rings are more distinct for the HiPIMS film (inset in Fig. 3d) and this is a sign of short-range order. Four ring radii, 0.23, 0.21, 0.14, and 0.12 nm, have been marked, and they can be attributed to the (111), (200), (220) and (311) reflections from the cubic CrC_x phase.

Hence, the TEM analysis confirmed the XRD results (Fig. 4). The carbide structure is concluded to be mainly amorphous CrC_y (a-CrC_y) with some occurrence of metastable nanocrystalline CrC_x grains (nc-CrC_x) with NaCl structure, up to 3 nm in size.

3.2.4. X-ray photoelectron spectroscopy

The XPS C1s peak from the films showed at least two separate peaks at about 283 eV and 284.5 eV. One example is shown in the inset in the bottom right corner of Fig. 6a. The peak at ~283 eV can be directly assigned to C–Cr bonds while the peak at ~284.5 eV can be attributed to C–C bonds. Hence, it can be concluded that the films are nanocomposites of a carbide component mixed with amorphous carbon (a-C:H). The Cr2p region was similar for all films and it is known that the Cr–Cr and Cr–C contributions appear at practically identical binding energies [34,38,39].

In many published papers on metal carbide films, the C–C peak is separated into sp^2 and sp^3 hybridized sub-peaks [17,39–41]. Furthermore, it is known that the interface between a carbide grain and a-C:H matrix can cause shifts in the C–Me peaks, giving rise to a C–Me* feature between the main C–Me and C–C peaks [5,42,43]. Our experimental data was, however, too limited to physically support a C–Cr* chemical environment. We have therefore applied three asymmetric Gaussian–Lorentzian (30% GL) peaks, at 283.0 ± 0.1 (C–Cr), 284.4 ± 0.1 (C sp^2), and 285.3 ± 0.1 (C sp^3) eV with acceptable result (i.e. low $\sum X^2$). Full widths at half maximum were 1.0 ± 0.1 eV for the carbide peak and 1.4 ± 0.1 eV for the two C–C peaks. It was found that the sp^2 fit accounted for 85–90% of the C–C intensity, and therefore the sum of
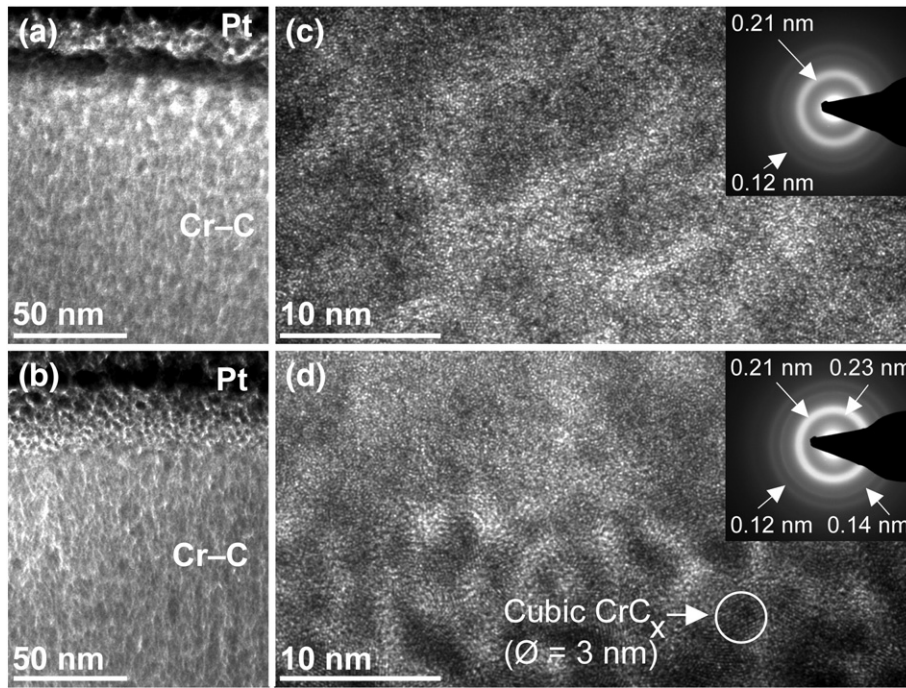
Fig. 5. TEM images for two Cr–C films with 56 at.% C. The letters correspond to (a) DCMS at low magnification, (b) HiPIMS at low magnification, (c) DCMS at high magnification, and (d) HiPIMS at high magnification. SAED patterns are shown as insets in (c) and (d).

the sp^2 and sp^3 sub-peaks will be used to represent the C–C peak. From the curve fits it is then straight-forward to calculate the relative amount of carbide phase (originating from both the a-CrC_y phase and the cubic nc-CrC_x phase), as well as a-C:H phase ($sp^2 + sp^3$), as a function of the total carbon content in the films. This is shown in Fig. 6a. As can be seen, the a-C:H phase content increases linearly from below 10%, which can be considered practically nothing, for films with a carbon content of ~20–25 at.% C, up to 84% for films with ~70 at.% C. Both the DCMS and the HiPIMS process resulted in an identical relationship. In Fig. 6a, we have also added some data from literature. Differences related to the 3d and 4d transition metals will be discussed below.

From Fig. 6a, the stoichiometry of the carbide component can be calculated by dividing the total carbidic carbon content with the total Cr content (assuming that all Cr forms carbide). The average $C_{carbidic}$/Cr ratio as a function of carbon content is shown in Fig. 6b. A peak maximum, where the ratio is 0.56, can be observed at a carbon content

of 50 at.% C. The experimental differences between DCMS and HiPIMS are considered insignificant.

3.2.5. Raman spectroscopy

Raman spectroscopy was used to qualitatively study the sp^2-rich carbon phase. Two representative spectra are shown in Fig. 7, and spectra for other films, including ones deposited at $U_b = -150$ V, were similar. Overall, the shape of the spectra corresponds to hydrogenated graphite-like carbon (GLCH) films with ~16–35 at.% H as reported by Casiraghi et al. [44]. The rather broad G peaks also indicate mainly small aromatic clusters less than 10 Å in size [45]. This result is in agreement with C–C bonds, detected by XPS, and in agreement with the incorporation of hydrogen, detected by NRA. The consequence of a GLCH phase on film properties should include a polymeric-like character, featuring e.g. low hardness and low elastic modulus.
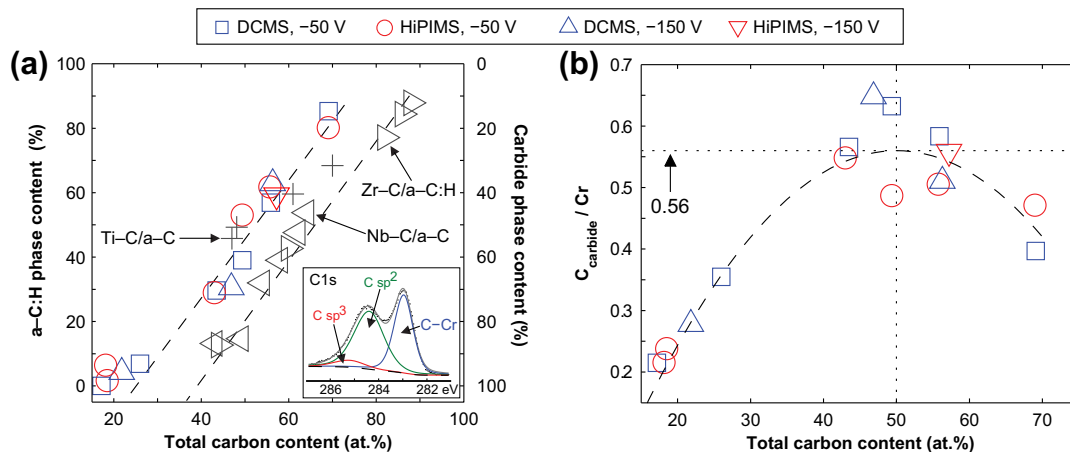

Fig. 6. (a) Relative phase content of a-C:H phase (C–C bonds) and carbide phase (C–Cr bonds) from XPS C1s peak deconvolutions plotted vs. the total carbon content. The phase contents for related carbide nanocomposites are also shown and were adapted from the works of Lewin et al. [5], Meng et al. [47], and Nedfors et al. [11]. The inset shows one XPS C1s spectrum obtained after 200 eV Ar^+ sputtering to a depth of ~8 nm for a Cr–C/a-C:H film with 56 at.% C. The circles are the raw data while the lines are the peak deconvolutions and their sum. (b) The $C_{carbidic}$/Cr ratio as a function of the total carbon content. The dashed lines in (a) and (b) are guides for the eye.
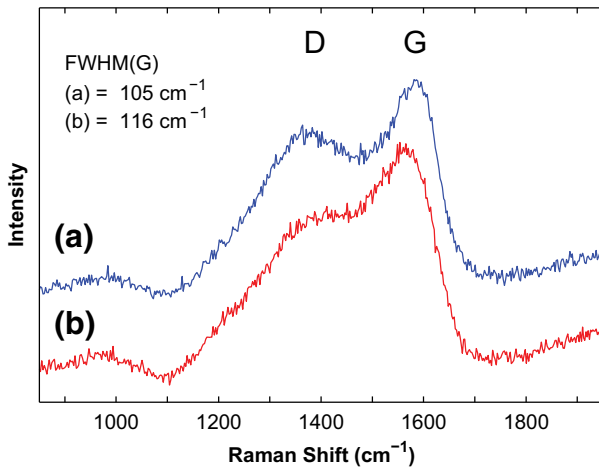
Fig. 7. Raman spectra for Cr–C/a-C:H films with 56 at.% carbon deposited by (a) DCMS and (b) HiPIMS. Laser wavelength was 514.5 nm. The peaks are marked D and G according to standard practice [43]. Spectra have been normalized relative to G peak intensity.

3.3. Characterization of functional film properties

3.3.1. Mechanical properties

Panels a and b in Fig. 8 show nanoindentation hardness and elastic modulus, respectively, as a function of the a-C:H phase content. Hardness is in the range 5.5–13 GPa and elastic modulus is in the range 66–230 GPa. Both parameters generally decrease with an increase in the a-C:H phase content for films deposited at $U_b = -50$ V. The DCMS and HiPIMS processes produced films with similar hardness values. However, the elastic modulus is clearly lower for the HiPIMS films (except at 60% a-C:H phase). Moreover, there is a rapid drop in elastic modulus when going from less than 10% a-C:H phase up to 30%. In the case of HiPIMS, the elastic modulus drops from 200 to 125 GPa. At about 80% a-C:H phase the HiPIMS film has an elastic modulus of only 65.8 ± 2.8 GPa. The film deposited by HiPIMS at $U_b = -150$ V deviates from the stated trends. It has 47% higher hardness (12.5 GPa) and 24% higher elastic modulus (171 GPa) compared to the film deposited at $U_b = -50$ V.

The hardness/elastic modulus (H/E) ratio is a parameter which corresponds to the elastic strain to failure and can be used to predict wear resistance [46]. This ratio is shown in Fig. 8c. It is clear that the ratios were higher for the most carbon-rich films (H/E ≈ 0.085) compared to the most chromium-rich films (H/E ≈ 0.058). The local maxima at 30% a-C:H phase in the H/E plots, corresponding to the drop in elasticity, have questionable significance and demonstrate the need for error analysis in these types of assessments.

In Fig. 8 we have also added data for non-reactively sputtered a-CrC_y/a-C films adapted from the works of Andersson et al. [13]. These results will be discussed below.

3.3.2. Tribological properties

Fig. 9a shows the evolution of friction coefficients (μ) as a function of the number of sliding cycles. Friction stabilizes to μ ≈ 0.15 after 500 cycles for the films with ~80% a-C:H phase, while the films with ~30% a-C:H phase have a higher μ of about 0.35. Friction coefficients depended almost linearly on the a-C:H phase content and this relationship is illustrated in Fig. 9b. The lowest average μ is 0.13 (average of 500 cycles). The difference in friction (μ = 0.4 < 0.6) between the two DCMS and HiPIMS films that were essentially without a-C:H phase may be due to their different columnar microstructures. Two SEM images, with a combination of elemental and topological contrast to clearly illustrate the wear tracks, are shown as insets. The film with about 80% a-C:H phase has much less Cr-based wear debris (bright areas) than the film without a-C:H phase. This result is a good sign of solid state lubrication by a carbon-rich,
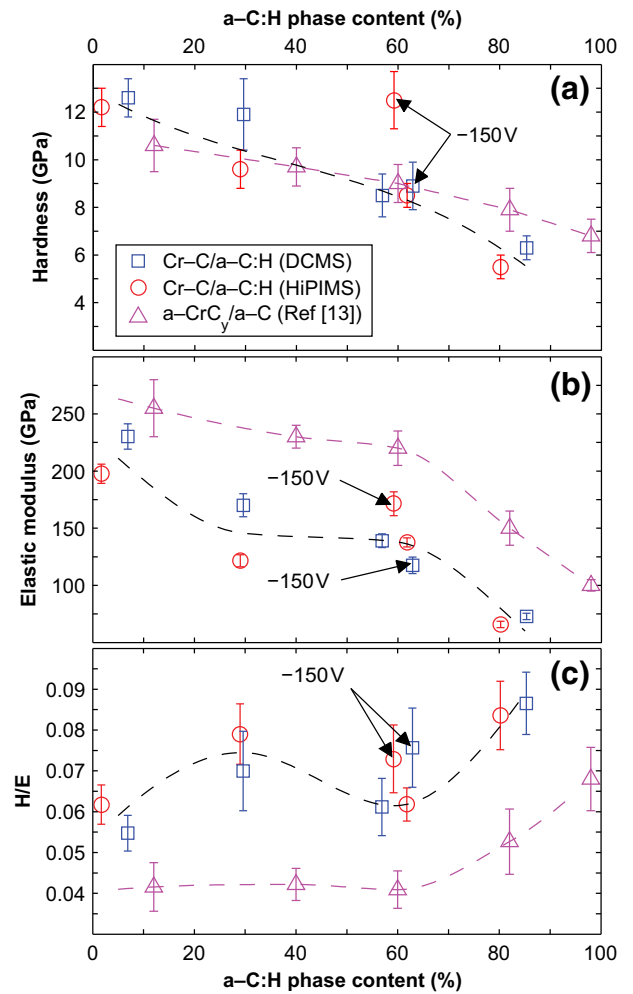

Fig. 8. Mean values and standard deviations for (a) nanoindentation hardness (H), (b) elastic modulus (E), and (c) H/E ratio for Cr–C/a-C:H films deposited by DCMS and HiPIMS as a function of a-C:H phase content. Films were deposited at a substrate bias potential (U_b) of −50 V unless marked differently. Values for a-CrC_y/a-C films (DCMS) were adapted from Andersson et al. [13]. The legend in (a) is valid for all sub-figures. The dashed lines are guides for the eye.

presumably graphitic, surface layer in the wear track on the former film, supported by its smooth appearance. Wear track widths were correlated to the a-C:H phase content, analogous to the friction coefficients.

3.3.3. Electrical contact properties

Electrical contact resistance as a function of the a-C:H phase content for films deposited on SS316L is shown in Fig. 10. Addition of a-C:H phase to single phase CrC_x reduced the contact resistance by two orders of magnitude. There is a clear minimum in the contact resistance for films with 30–60% a-C:H phase and the lowest contact resistance is 69 ± 15 mΩ. Additional a-C:H phase, about 80% in total, increased the contact resistance by one order of magnitude. Contact resistances for SS316L coated with 1 μm Ag and for uncoated SS316L were measured to be 13 ± 2 mΩ and 1.5 ± 1 Ω, respectively. The large error for the latter can be attributed to, presumably thick, native surface oxides.

4. Discussion

4.1. Microstructure

The results above show that the films consist of two types of phases: One hydrogenated amorphous carbon phase (a-C:H) and one Cr-rich
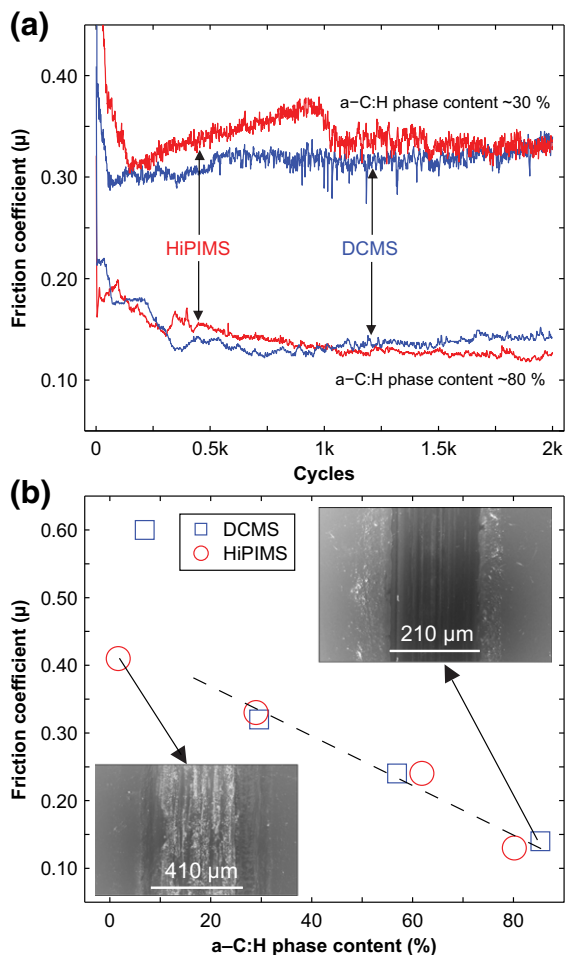
Fig. 9. (a) Friction coefficients for Cr–C/a-C:H films vs. the number of sliding cycles in a reciprocating sliding ball on flat surface experiment. Ball bearing 100Cr6 steel ball, Ø = 10 mm, 5 N normal load, no lubrication. The film substrate was SS316L. (b) Mean friction coefficient recorded from 1500 to 2000 cycles plotted vs. a-C:H phase content. Insets are SEM images of wear tracks after 2000 cycles.

carbide phase. In some films, this carbide phase is more or less completely amorphous (a-CrC$_x$), while nanocrystalline grains of metastable cubic CrC$_x$ (nc-CrC$_x$) are observed at other compositions. The relative amount of a-C:H phase increased linearly with an increase in total carbon content, which is a very typical trend for sputtered Me–C/a-C films. In Fig. 6a, we have added literature data from Lewin et al. [5], Meng et al. [47], and Nedfors et al. [11] on similar studies in the Ti–C, Zr–C and Nb–C systems, respectively. It is obvious that the trends for the 3d metals (Ti and Cr) are overlapping although the films were obtained at different deposition rates using different processes. In contrast, the two 4d transition metals form overlapping trends where a higher total carbon content in the film is required to obtain a given amount of a-C phase. The amount of a-C phase is typically related to the mean separation distance of carbide grains, where the separation distance also corresponds to a given number of atomic carbon layers. However, in order to perform this calculation [48] one needs to know the mean grain size, which is exceedingly difficult to obtain for mostly amorphous a-CrC$_y$. Mean grain separation distances for the more crystalline Nb–C/a-C and Ti–C/a-C film systems are about 0.5 and 2.5 nm, respectively [5,11]. Since Cr appears to group with Ti in Fig. 6a, a rather thick carbon matrix thickness would be expected, with e.g. low hardness as consequence. This is in good agreement with the low hardness values in Fig. 8a.

The carbide phase was mainly amorphous, although there was clear XRD and TEM evidence of a metastable cubic nc-CrC$_x$ phase as well.

Starting with the amorphous phase, this lack of order is very unusual for reactive sputtering as statistically suggested by Andersson et al. [13]. The latter authors noted that non-reactive sputtering tends to form more amorphous Cr–C films than reactive sputtering, where nanocrystalline structures are typically obtained. The very low structural order in our films can be explained by the high industrial deposition rates, which were two orders of magnitude higher compared with previously published studies on non-reactive [13,15,17,19,49] as well as reactive DCMS [34,50] of Cr–C films. Panjan et al. [50] as well as Gassner et al. [34] sputtered Cr–C films reactively at deposition rates of 13–25 nm·min^{-1}, roughly ten times lower than in the present study, and obtained carbide grains up to 10 nm in size (at 150 °C). The Cr–C system has not previously been studied using HiPIMS but it should be noted that the obtained deposition rates (50–125 nm·min^{-1}) were higher than the rates stated in the literature for DCMS (generally 5–50 nm·min^{-1}). Our high deposition rates likely quenched nucleation, but the question is then why the cubic nc-CrC$_x$ phase formed as well.

A stable Cr–C phase with NaCl structure cannot be expected from Hägg's empirical rule due to a ratio between the carbon and metal atom radii exceeding 0.59 [12]. Furthermore, the NaCl structure is known to become less stable going from group 4 transition metals to metals with more d-electrons [12]. This is due to filling of antibonding states, leading to a destabilization of the NaCl structure relative to other structures. Consequently, the stable Cr–C phases, such as Cr$_{23}$C$_6$, form other more complicated crystal structures with large unit cells, which require substantial surface diffusion to form during thin film growth. A sputtering process with a high quenching rate of adsorbed species, carried out at low substrate temperatures, gives very limited surface diffusion making it difficult to obtain such complex structures. This favors the formation of simple structures like the cubic (NaCl) nc-CrC$_x$ observed in our study. This phase is metastable due to the mentioned filling of antibonding states, but the stability is increased by the formation of carbon vacancies. In our films, we have two chromium carbide phases; the amorphous chromium carbide, a-CrC$_y$, and the metastable cubic nc-CrC$_x$. We cannot accurately determine the relative amount of the two carbide phases, and therefore we cannot calculate the exact stoichiometry of the nc-CrC$_x$ phase. However, we know that the overall C$_{carbidic}$/Cr ratio is 0.56 in a film with a total C/Cr ratio of 1 (Fig. 6b). From two previous studies [13,17] it can be concluded that y in a-CrC$_y$ should be in the range 0.3–0.54, while Bewilogua et al. [51] obtained cubic CrC$_x$ and expected x to be in the range 0.5 < x < 0.75. Since the literature suggests 0.3 < y < 0.54 for a-CrC$_y$ and 0.5 < x < 0.75 for nc-CrC$_x$, our
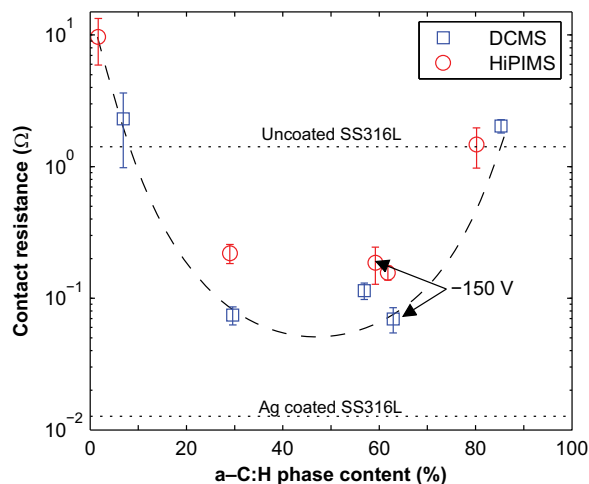

Fig. 10. Electrical contact resistance for Cr–C/a-C:H films vs. a-C:H phase content. Counterpart was an Au/Ni plated spring-loaded test probe (Ø = 1.2 mm) and the contact force was 1.00 ± 0.01 N. Contact resistances of uncoated SS316L and Ag coated SS316L are illustrated by the two horizontal dotted lines. The dashed line is a guide for the eye.

average value of $CrC_{0.56}$ is a reasonable trade-off from a mixture of the two phases with carbon vacancies in the nc-CrC_x phase.

The use of DCMS or HiPIMS did not affect the phase contents of chromium carbide and amorphous carbon at any given composition. This result is different compared to the Ti–C system, where Samuelsson et al. [43] observed films with more Ti – C bonds and fewer C – C bonds for HiPIMS than DCMS. However, there is a major difference in glass forming ability between the Cr-C and Ti-C systems, and any similar promotion of carbide phase due to HiPIMS may be more limited when growing Cr–C films. In fact, the only major difference between the DCMS and HiPIMS films is in their morphologies (Figs. 2 and 3), where film growth by the HiPIMS process is clearly denser. Further tuning of the process conditions, in particular the current density and the substrate bias potential, may extend these differences.

4.2. Properties of the films

Hardness and elastic modulus were generally low for being carbide-based nanocomposite films. In Fig. 8a, hardness can be compared to that of similar a-CrC_y/a-C films (i.e. hydrogen free) reported by Andersson et al. [13]. Overall the hardness values are quite similar, although it may be interpreted that our films are a few GPa harder at less than 40% a-C:H phase, and a few GPa softer at about 80% a-C:H phase. Considering that all these films are mainly amorphous, their similarly low hardness is not that surprising. However, the HiPIMS film deposited at $U_b = -150$ V had much higher hardness (as well as higher elastic modulus as seen in Fig. 8b). There is no difference in the carbide phase content (Fig. 6a) or in the XRD diffractograms (Fig. 4) to account for this increase. The TEM analysis (Fig. 5), however, indicates that the HiPIMS film may have more nc-CrC_x phase, which would explain the increase in hardness. The SEM micrographs (Figs. 2 and 3) suggest film densification and a more refined surface structure as probable cause, while another possibility may be higher compressive stresses. A comparison of the elastic moduli (Fig. 8b) for our films to the non-reactively sputtered films [13] shows that our films have lower elastic modulus at any given a-C:H phase content. Since the trends in Fig. 8b appear to converge for 0% a-C(:H) phase, the lower elastic modulus can be attributed to the GLCH-type carbon in our films. The low elastic moduli are in agreement with the predictions made from the Raman results in Section 3.2.5 (Fig. 7).

It is well known that crystalline films have both higher hardness and higher elastic modulus than amorphous films due to their different deformation behaviors. Hardness and elastic modulus can then be compared to other Me–C systems where a nanocrystalline nc-MeC_x phase is normally obtained. For example, hardness values for nc-TiC_x/a-C and nc-NbC_x/a-C films are about 15 and 25 GPa, respectively, at a carbon content of about 50 at.% C [11]. Both values are considerably higher than the 9 GPa found for our films at a similar carbon content (Fig. 8a). Meanwhile, the elastic modulus for the above Ti and Nb-based films is about 290 GPa [11], which is roughly twice as high compared to our films. It is thus clear that the amorphous carbide as well as the hydrogenated amorphous carbon phase correspond to both the low hardness and the low elastic modulus.

Although the hardness was relatively low, it is probably sufficient for the intended electrical contact applications. In fact, a sufficient hardness and a low elastic modulus are a promising combination because the hardness over elastic modulus (H/E) ratio is an indicator for good wear properties [52,53]. With a high H/E ratio, the film surface can respond to an external force by elastic recovery rather than plastic deformation and thus reduce wear [54]. As was shown in Fig. 8c, the H/E ratio increases with an increase in carbon content and this is a typical trend for Me–C films [11,47,55]. The smooth wear track in Fig. 9b (top inset) corresponds to a high carbon content and a high H/E ratio. Conversely, the wear track with a lot of wear debris in Fig. 9b (bottom inset) corresponds to a low carbon content and a low H/E ratio. In Fig. 8c it also becomes apparent that the reactively sputtered films

have higher H/E ratios than the non-reactively sputtered films. A similar effect can be expected for other Me–C systems as well, suggesting that reactive sputtering will yield films that are more suitable for wear applications.

Although the highest H/E ratios were found for the most carbon-rich films, an electric contact application would probably require more metal in the films for adequate electrical properties. It is then interesting to study how some different Me–C films would rank by their H/E ratios at more moderate carbon contents. If Me–C films with a carbon content of about 40–45 at.% C are considered, the order for Ti, Cr, Zr, and Nb is (from low to high H/E): Ti–C (0.042) < Zr–C (0.063) < Nb–C (0.069) < Cr–C (0.075) [11,47]. This ranking suggests that the Cr–C system can give films with good wear properties. However, further studies are required to reveal if there is any systematic trend between the different Me–C systems, or if it is just a matter of different deposition conditions (substrate, film thickness, etc.).

The friction coefficient in our films is strongly dependent on the amount of a-C phase as shown in Fig. 9b. This trend is typical for Me–C/a-C films and has been observed in many studies for a large range of metals such as Ti, Zr, Nb, Ta, and W [4,47,55,56]. The reduction in friction is well known and due to the presence of a lubricating graphite-like tribofilm, whose formation is more favorable with a larger content of a-C phase in the films [56]. In particular, Gassner et al. [20] demonstrated surface graphitization during sliding for nc-CrC_x/a-C:H films. Our friction results are similar to the literature, although it is difficult to compare results from different studies due to different experimental deposition and sliding conditions.

A sliding electrical contact application, however, requires not only a low friction coefficient, but also a low contact resistance. As can be seen in Fig. 10, the lowest contact resistance, not that much higher than the Ag reference, is obtained when 30 and 60% of the carbon exists as a-C:H phase. The explanation for the minimum was not resolved, but may include thin surface oxides at moderate a-C:H phase content [17], whereas excessive a-C:H phase may impair conductivity [13]. An alternative possibility suggested by Lewin et al. [5] is that the minimum in contact resistance is attributed to an optimal thickness of the a-C phase separating the carbide grains. As we were unable to estimate the carbide grain sizes, further investigations are required to explain the minimum. Either way, the films with the lowest contact resistance had somewhat higher friction coefficients (0.2–0.3, Fig. 9b) than the most carbon-rich films. These two results jointly indicate a trade-off situation between low contact resistance and low friction. Nonetheless, this range in a-C:H phase will likely yield nanocomposite films with a high corrosion resistance [17]. Low friction, good wear properties, low contact resistance, and high corrosion resistance are things that make the present Cr–C/a-C:H films very interesting candidates for sliding electrical contacts.

5. Conclusions

Nanocomposite chromium carbide/hydrogenated amorphous carbon (Cr–C/a-C:H) films were deposited by high rate reactive DCMS and HiPIMS at a substrate temperature of 126 ± 26 °C. Phase contents were linked to the total carbon content, which was controlled by the C_2H_2 flow rate. The carbide phase was mainly amorphous a-CrC_y with minor incorporation of metastable cubic nc-CrC_x up to 3 nm in grain size. The a-C:H phase was similar to sp^2-rich hydrogenated graphite-like amorphous carbon (GLCH) films. Overall, the DCMS and HiPIMS processes yielded films with similar phase contents and microstructures, as well as similar functional properties. Nanoindentation hardness and elastic modulus were in the ranges 5.5–13 GPa and 66–230 GPa, respectively. Unlubricated friction coefficients down to 0.13 were obtained for films with 69 at.% carbon. Electrical contact resistance vs. an Au/Ni probe was found to dramatically depend on the a-C:H phase content, where 30–60% a-C:H phase yielded the lowest contact

resistance. The present nanocomposite Cr–C films are potential candidates for use in sliding electrical contact applications.

Conflict of interest

The authors declare that there are no conflicts of interest.

Acknowledgment

References

[1] M. Antler, Thin Solid Films 84 (1981) 245–256.
[2] J.F. Archard, W. Hirst, Proc. R. Soc. A Math. Phys. Eng. Sci. 236 (1956) 397–410.
[3] Å. Öberg, Å. Kassman, B. André, U. Wiklund, E. Lewin, et al., Eur. Phys. J. Appl. Phys. 49 (2009) 22902.
[4] H. Dimigen, C.-P. Klages, Surf. Coat. Technol. 49 (1991) 543–547.
[5] E. Lewin, O. Wilhelmsson, U. Jansson, J. Appl. Phys. 100 (2006) 054303.
[6] E. Lewin, B. André, S. Urbonaite, U. Wiklund, U. Jansson, J. Mater. Chem. 20 (2010) 5950.
[7] J. Lauridsen, P. Eklund, T. Joelsson, H. Ljungcrantz, Å. Öberg, E. Lewin, et al., Surf. Coat. Technol. 205 (2010) 299–305.
[8] J. Lauridsen, P. Eklund, J. Jensen, H. Ljungcrantz, Å. Öberg, E. Lewin, et al., Acta Mater. 58 (2010) 6592–6599.
[9] J. Lauridsen, P. Eklund, J. Jensen, A. Furlan, A. Flink, A.M. Andersson, et al., Thin Solid Films 520 (2012) 5128–5136.
[10] N.G. Sarius, J. Lauridsen, E. Lewin, U. Jansson, H. Högberg, Å. Öberg, et al., J. Electron. Mater. 41 (2011) 560–567.
[11] N. Nedfors, O. Tengstrand, E. Lewin, A. Furlan, P. Eklund, L. Hultman, et al., Surf. Coat. Technol. 206 (2011) 354–359.
[12] U. Jansson, E. Lewin, Thin Solid Films 536 (2013) 1–24.
[13] M. Andersson, J. Högström, S. Urbonaite, A. Furlan, L. Nyholm, U. Jansson, Vacuum 86 (2012) 1408–1416.
[14] M. Magnuson, M. Andersson, J. Lu, L. Hultman, U. Jansson, J. Phys. Condens. Matter 24 (2012) 225004.
[15] S. Groudeva-Zotova, R.G. Vitchev, B. Blanpain, Surf. Interface Anal. 30 (2000) 544–548.
[16] G. Gassner, P. Mayrhofer, C. Mitterer, J. Kiefer, Surf. Coat. Technol. 200 (2005) 1147–1150.
[17] K. Nygren, et al., Appl. Surf. Sci. (2014), http://dx.doi.org/10.1016/j.apsusc.2014.03.014.
[18] N. Maréchal, Y. Pauleau, S. Païdassi, Surf. Coat. Technol. 54–55 (1992) 320–323.
[19] N. Maréchal, E. Quesnel, Y. Pauleau, J. Mater. Res. 9 (1994) 1820–1828.
[20] G. Gassner, J. Patscheider, P.H. Mayrhofer, S. Šturm, C. Scheu, C. Mitterer, Tribol. Lett. 27 (2007) 97–104.
[21] C. Mitterer, M. Lechthaler, G. Gassner, G.A. Fontalvo, L. Tóth, B. Pécz, et al., Proc. Inst. Mech. Eng. Part J J. Eng. Tribol. 223 (2009) 751–757.
[22] M. Keunecke, K. Bewilogua, J. Becker, A. Gies, M. Grischke, Surf. Coat. Technol. 207 (2012) 270–278.
[23] M. Samuelsson, D. Lundin, K. Sarakinos, F. Björefors, B. Wälivaara, H. Ljungcrantz, et al., J. Vac. Sci. Technol. A 30 (2012) 031507.
[24] H. Ljungcrantz, T. Rosell, Device for carrying out a surface treatment of substrates under vacuum, US 7,993,456 B2, 2011.
[25] R.M. Langford, A.K. Petford-Long, J. Vac. Sci. Technol. A 19 (2001) 2186.
[26] E. Lewin, M. Gorgoi, F. Schäfers, S. Svensson, U. Jansson, Surf. Coat. Technol. 204 (2009) 455–462.
[27] A. Zalar, J. Kovac, B. Pracek, P. Panjan, M. Ceh, Vacuum 82 (2007) 116–120.
[28] J. Benedikt, D.C. Schram, M.C.M. van de Sanden, J. Phys. Chem. A 109 (2005) 10153–10167.
[29] J.T. Gudmundsson, J. Alami, U. Helmersson, Surf. Coat. Technol. 161 (2002) 249–256.
[30] I. Petrov, P.B. Barna, L. Hultman, J.E. Greene, J. Vac. Sci. Technol. A 21 (2003) S117.
[31] A.P. Ehiasarian, Pure Appl. Chem. 82 (2010) 1247–1258.
[32] G. Greczynski, J. Jensen, L. Hultman, IEEE Trans. Plasma Sci. 38 (2010) 3046–3056.
[33] L. Yate, L. Martínez-de-Olcoz, J. Esteve, A. Lousa, Surf. Coat. Technol. 206 (2012) 2877–2883.
[34] G. Gassner, J. Patscheider, P.H. Mayrhofer, E. Hegedus, L. Tóth, I. Kovacs, et al., J. Vac. Sci. Technol. B 24 (2006) 1837–1843.
[35] T. Zehnder, J. Patscheider, Surf. Coat. Technol. 133–134 (2000) 138–144.
[36] B.X. Liu, X.Y. Cheng, J. Phys. Condens. Matter 265 (1992).
[37] W. Dai, G. Wu, A. Wang, Diamond Relat. Mater. 19 (2010) 1307–1315.
[38] V. Singh, J. Jiang, E. Meletis, Thin Solid Films 489 (2005) 150–158.
[39] W. Dai, P. Ke, A. Wang, Vacuum 85 (2011) 792–797.
[40] J. Díaz, G. Paolicelli, S. Ferrer, F. Comin, Phys. Rev. B 54 (1996) 8064–8069.
[41] K. Zhang, M. Wen, G. Cheng, X. Li, Q.N. Meng, J.S. Lian, et al., Vacuum 99 (2014) 233–241.
[42] E. Lewin, P. Persson, M. Lattemann, M. Stuber, M. Gorgoi, A. Sandell, et al., Surf. Coat. Technol. 202 (2008) 3563–3570.
[43] M. Samuelsson, K. Sarakinos, H. Högberg, E. Lewin, U. Jansson, B. Wälivaara, et al., Surf. Coat. Technol. 206 (2012) 2396–2402.
[44] C. Casiraghi, A.C. Ferrari, J. Robertson, Phys. Rev. B 72 (2005) 1–14.
[45] J. Schwan, S. Ulrich, V. Batori, H. Ehrhardt, S.R.P. Silva, J. Appl. Phys. 80 (1996) 440.
[46] A. Leyland, A. Matthews, Wear 246 (2000) 1–11.
[47] Q.N. Meng, M. Wen, F. Mao, N. Nedfors, U. Jansson, W.T. Zheng, Surf. Coat. Technol. 232 (2013) 876–883.
[48] T. Zehnder, P. Schwaller, F. Munnik, S. Mikhailov, J. Patscheider, J. Appl. Phys. 95 (2004) 4327.
[49] A. Paul, J. Lim, K. Choi, C. Lee, Mater. Sci. Eng. A 332 (2002) 123–128.
[50] P. Panjan, M. Cekada, D. Kek Merl, M. Macek, B. Navinsek, A. Jesih, et al., Vacuum 71 (2003) 261–265.
[51] K. Bewilogua, H. Heinitz, B. Rau, S. Schulze, Thin Solid Films 167 (1988) 233–244.
[52] A. Leyland, A. Matthews, Surf. Coat. Technol. 177–178 (2004) 317–324.
[53] S. Guruvenket, D. Li, J.E. Klemberg-Sapieha, L. Martinu, J. Szpunar, Surf. Coat. Technol. 203 (2009) 2905–2911.
[54] C.A. Charitidis, Int. J. Refract. Met. Hard Mater. 28 (2010) 51–70.
[55] Y. Pei, D. Galvan, J. Dehosson, Acta Mater. 53 (2005) 4505–4521.
[56] J.C. Sánchez-López, D. Martínez-Martínez, M.D. Abad, A. Fernández, Surf. Coat. Technol. 204 (2009) 947–954.